

# Multiparametric oxygen-enhanced functional lung imaging in 3D

Kathrin R. F. Hemberger · Peter M. Jakob ·  
Felix A. Breuer

Received: 13 May 2014/Revised: 12 September 2014/Accepted: 15 September 2014/Published online: 9 October 2014  
© ESMRMB 2014

## Abstract

**Objective** To develop a self-gated free-breathing 3D sequence allowing for simultaneous  $T_1$ -weighted imaging and quantitative  $T_2^*$  mapping in different breathing phases in order to assess the feasibility of oxygen-enhanced 3D functional lung imaging.

**Materials and methods** A 3D sequence with ultrashort echo times and interleaved double readouts was implemented for oxygen-enhanced lung imaging at 1.5 T. Six healthy volunteers were examined while breathing room air as well as 100 % oxygen. Images from expiratory and inspiratory breathing phases were reconstructed and compared for the two breathing gases.

**Results** The average  $T_2^*$  value measured for room air was 2.10 ms, with a 95 % confidence interval (CI) of 1.95–2.25 ms, and the average for pure oxygen was 1.89 ms, with a 95 % CI of 1.76–2.01 ms, resulting in a difference of 10.1 % (95 % CI 8.9–11.3 %). An 11.2 % increase in signal intensity (95 % CI 10.4–12.1 %) in the  $T_1$ -weighted images was detected when subjects were breathing pure oxygen compared to room air. Furthermore, a significant change in signal intensity (26.5 %, 95 % CI 18.8–34.3 %) from expiration to inspiration was observed.

**Conclusions** This study demonstrated the feasibility of simultaneous  $T_2^*$  mapping and  $T_1$ -weighted 3D imaging of the lung. This method has the potential to provide information about ventilation, oxygen transfer, and lung expansion within one experiment. Future studies are needed to investigate the clinical applicability and diagnostic value of this approach in various pulmonary diseases.

**Keywords** Lung imaging ·  $T_2^*$ -mapping ·  $T_1$ -weighted imaging · Oxygen-enhanced · Ultrashort echo time

## Introduction

In recent years, several groups have demonstrated that functional lung MRI using inhaled oxygen as a contrast medium can be obtained using a clinical MR scanner. These methods are largely based on measuring differences in  $T_1$  or  $T_1$ -weighted images [1–7] with subjects breathing pure oxygen compared to room air. As pure oxygen is weakly paramagnetic, a  $T_1$  shortening is observed when subjects are breathing pure oxygen versus breathing room air due to an increased concentration of oxygen in the air spaces and blood vessels. The detected signal changes result from the process of oxygen transfer involving three mechanisms—ventilation, diffusion, and perfusion—which together are described as the oxygen transfer function (OTF).

Recently, quantification of  $T_2^*$  was introduced as a complementary technique to obtain functional lung information. In diseases of the lung, impaired oxygen uptake affects the local oxygen concentration in the alveoli, which is reflected in a change in magnetic susceptibility at the gas-tissue interface, and thus a change in  $T_2^*$ . The utility of

K. R. F. Hemberger (✉) · P. M. Jakob · F. A. Breuer  
Research Center Magnetic-Resonance-Bavaria (MRB),  
Am Hubland, 97974 Wuerzburg, Germany  
e-mail: kathrin.hemberger@mr-bavaria.de

P. M. Jakob  
e-mail: peja@physik.uni-wuerzburg.de

F. A. Breuer  
e-mail: breuer@mr-bavaria.de

P. M. Jakob  
Department of Experimental Physics 5, University of  
Wuerzburg, Am Hubland, 97974 Wuerzburg, Germany

regional  $T_2^*$  measurement for assessment of pulmonary diseases was previously demonstrated [8, 9].

Since the difference in magnetic susceptibility between blood and air space depends on the concentration of oxygen in the respiratory gas, a reduction in  $T_2^*$  can be expected with oxygen-enhanced imaging. Pracht et al. [10] measured a decrease of approximately 10 % in  $T_2^*$  under hyperoxic conditions, demonstrating the potential of  $T_2^*$  as a new contrast mechanism for oxygen-enhanced functional lung imaging. They attributed this change in  $T_2^*$  to the increased difference in susceptibility between the gas in the alveoli and the surrounding tissue, and concluded that this approach presented a more direct route for ventilation imaging compared to  $T_1$ .

The purpose of this study was the simultaneous assessment of both enhancement mechanisms in 3D imaging to obtain broader information about the functionality in the whole lung. Evaluation of  $T_1$ -weighted imaging together with quantitative  $T_2^*$  measurements, which enables the correlation of information regarding ventilation and oxygen uptake, may deliver more accurate information about lung functionality, and is therefore of high clinical and scientific interest. For example, measuring both  $T_2^*$  maps and  $T_1$ -weighted images together at different concentrations of oxygen in the breathing gas has the potential to allow for evaluation of ventilation/perfusion (V/Q) mismatch without the need for contrast agents. V/Q mismatch is a major cause of disturbances in blood gas levels, often leading to clinical hypoxia, or low blood oxygen. In  $T_1$ -weighted images, the V/Q mismatch results in homogeneous enhancement of signal intensity in response to oxygen in the whole lung [13]. Together with the quantitative  $T_2^*$  maps, the proposed method has the potential to identify impaired areas and indicate the presence of ventilation/perfusion mismatch.

However,  $^1\text{H}$  MRI of the lung poses significant challenges, with issues arising from cardiac and respiratory motion, low proton density, and very fast signal decay. Standard gradient-echo sequences and single-shot fast spin-echo sequences with short echo times (TE) have both been used for MRI of the lung [11, 12]. In addition, radial acquisitions that provide ultrashort echo time (UTE) have the proven ability to image the parenchyma with higher signal intensity than standard methods [8, 13]. The ultrashort echo time provides more signals from tissues with short  $T_2^*$ , such the parenchyma, and offers the potential for direct detection of lung tissue destruction. The ability of regional  $T_2^*$  measurements with 3D PR to detect pulmonary diseases has been reported in animal models [8] as well as in human subjects [9]. The utility of oxygen-enhanced  $T_1$ -weighted 3D UTE for functional imaging was demonstrated in a rat model [14] and

recently in human subjects [6, 7]. The drawback of radial acquisitions is the nonuniform sampling density of the  $k$ -space, which increases the image noise [15] and requires a large number of projections for adequate  $k$ -space coverage. Density-adapted (DA) sequences, in which the gradient is designed to keep the average sampling density constant, provide higher scan efficiency and have been shown to be of benefit for lung imaging [16]. Johnson et al. [16] used a 3D DA-UTE sequence for high-resolution structural lung imaging, and reported reduced blurring artefacts, more efficient  $k$ -space sampling, and higher signal-to-noise ratio (SNR). Further improved scan efficiency can be achieved with twisted projection imaging (TPI), which significantly reduces the total number of projections required to fulfill the Nyquist criterion [17], and thus is favorable for oxygen-enhanced  $T_2^*$  measurement in 3D.

In this study, we employed a pulse sequence that provides the enhanced sampling efficiency of TPI combined with retrospective respiratory self-gating. Retrospective gating methods have been shown to be robust toward unstable gating signals and irregular breathing, and have the advantage over prospective gating methods to generate arbitrary respiratory phases (e.g. expiration and inspiration) [18].  $T_1$ -weighted signal intensity (SI) and quantitative  $T_2^*$  values were calculated from a multi-echo sequence and compared for different breathing gases and different breathing states in six healthy volunteers.

## Materials and methods

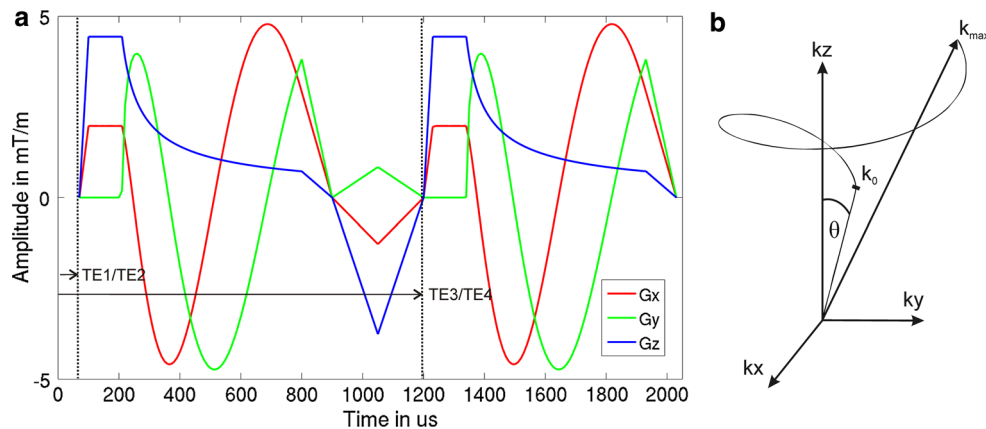
### Sequence design

Figure 1a shows the gradient trajectory of the proposed multi-echo TPI sequence. Since the  $T_2^*$  of the lung parenchyma is very short at 1.5 T, sampling multiple readouts in a single TR is not adequate to cover the complete  $T_2^*$  decay. Therefore, two interleaved double readouts were used. The first double readout acquired data at echo times of 0.07 ms and 1.2 ms. In the next TR, data was acquired at echo times of 0.6 ms and 1.73 ms.

Figure 1b shows the corresponding cone-shaped  $k$ -space trajectory. Each trajectory starts at the  $k$ -space center as a radial line up to a predefined  $k$ -space fraction  $p$  at  $k_0 = pk_{\text{max}}$ , and then twists to maintain a constant sampling density according to the following equations [17]:

$$k(t) = \sqrt[3]{3\gamma k_0^2 G + k_0^3}$$

$$\sigma = \sqrt{\frac{k(t)^4}{k_0^4} - 1}$$



**Fig. 1** Density-adapted gradient trajectories  $G_x$  (red),  $G_y$  (green), and  $G_z$  (blue) of the proposed multi-echo TPI sequence, consisting of first readout followed by a short rephaser gradient and second readout (a). Dashed vertical line illustrates the time points of data acquisition. Data at  $TE_1 = 70 \mu\text{s}$  and  $TE_3 = 1,200 \mu\text{s}$  were acquired in one TR.

$$\Phi(t) = \frac{(\sigma - \arctan \sigma)}{2 \sin \theta}$$

with gyromagnetic ratio  $\gamma$ , polar angle  $\theta$  ( $0 < \theta < \pi$ ), and azimuth angle  $\Phi$  ( $0 < \Phi < 2\pi$ ). The factor  $p$  is the part of  $k$ -space that is linearly sampled, and reduces the Nyquist radius and thus the number of projections needed for fully sampled data. The minimum value of  $p$  and the desired gradient shapes are limited by maximal gradient strength and slew rate. An iterative method was used to generate efficient gradient waveforms. The method automatically computes optimal gradient waveform (ramp-up-time,  $k_0$ ) for a given readout length, field of view (FOV), and resolution in order to reach  $k_0$  most rapidly. In contrast to the original TPI, where a new  $k$ -space trajectory is calculated for each projection, only one cone-shaped trajectory is employed. The whole  $k$ -space is then covered by rotating the same cone by the projection angles  $\vartheta$  ( $0 < \vartheta < \pi$ ) and  $\varphi$  ( $0 < \varphi < 2\pi$ ) [19].

To achieve a flexible sampling in time, a series of  $N_{\text{proj}}$  quasi-random 2D Niederreiter numbers  $\lambda_1$  ( $0 < \lambda_1 \leq 1$ ) and  $\lambda_2$  ( $0 < \lambda_2 \leq 1$ ) [18] were generated to determine the azimuth angle  $\vartheta = \arccos(2\lambda_1 - 1)$  and the polar angle  $\varphi = 2\pi\lambda_2$ , respectively [20]. This approach generates an approximately uniform distribution of the projections and broadens the reconstruction to any temporal window.

### Density compensation function

Reconstruction of MRI images from data sampled on arbitrary  $k$ -space trajectories requires a determination of the sampling density compensation function (DCF). To demonstrate the homogeneous sampling density of TPI, the

In the next TR, all gradients were shifted in time by  $530 \mu\text{s}$  to acquire data at  $TE_2 = 600 \mu\text{s}$  and  $TE_4 = 1,730 \mu\text{s}$ . Corresponding  $k$ -space trajectory (b) with cone-angle  $\theta$  twists between  $k_0$  and  $k_{\text{max}}$  so that a constant sampling density was achieved

DCF was simulated and compared with 3D UTE and 3D DA-UTE, given the same spatial resolution ( $128 \times 128 \times 128$ ), for a fully sampled (60,000 projections) and an undersampled (10,000 projections) case (Fig. 2). In 3D UTE, the sampling density is  $\propto 1/k^2$ , and as expected, shows a non-constant DCF  $\propto k^2$ . In 3D DA-UTE, the non-constant sampling density is compensated after  $k_0 = pk_{\text{max}}$  in the radial direction, resulting in a constant DCF for the fully sampled case. As 3D DA-UTE does not provide constant sampling density in the angular direction, the DCF needs to be adapted in the undersampled case; data beyond the Nyquist radius are weighted less by employing an additional low-pass filter such that undersampling artefacts are suppressed, resulting in a loss of image resolution. In contrast, TPI already delivers constant sampling density in the radial and the angular direction at a smaller number of projections. Thus, no density compensation is required above  $k_0$ , and no low-pass filter must be applied, thereby providing full image resolution. In this study, the appropriate DCFs, including low-pass filtering in the case of undersampling, were calculated according to the criterion proposed by Pipe et al. [21].

### Retrospective gating

Given the long acquisition times required for 3D imaging, the use of breath-hold acquisitions in this setting is impractical. Instead, a retrospective gating approach using the  $k$ -space center (DC) signal [18, 22] offers the advantage of reconstructing images in expiratory and inspiratory phases. Since every  $k$ -space trajectory starts at the center of the  $k$ -space, the DC signal is intrinsically available with each projection. Respiratory and cardiac motions induce changes in the DC signal, which can thus be used for

**Fig. 2** Central section of simulated DCF of 3D UTE, 3D DA-UTE, and TPI for  $6 \times 10^4$  (fully sampled case, **a**) and  $10^4$  (undersampled case, **b**) projections. Note the constant sampling density for TPI

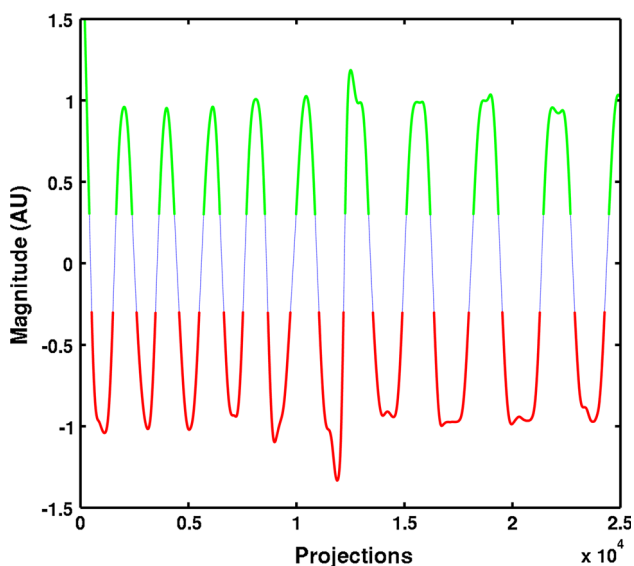
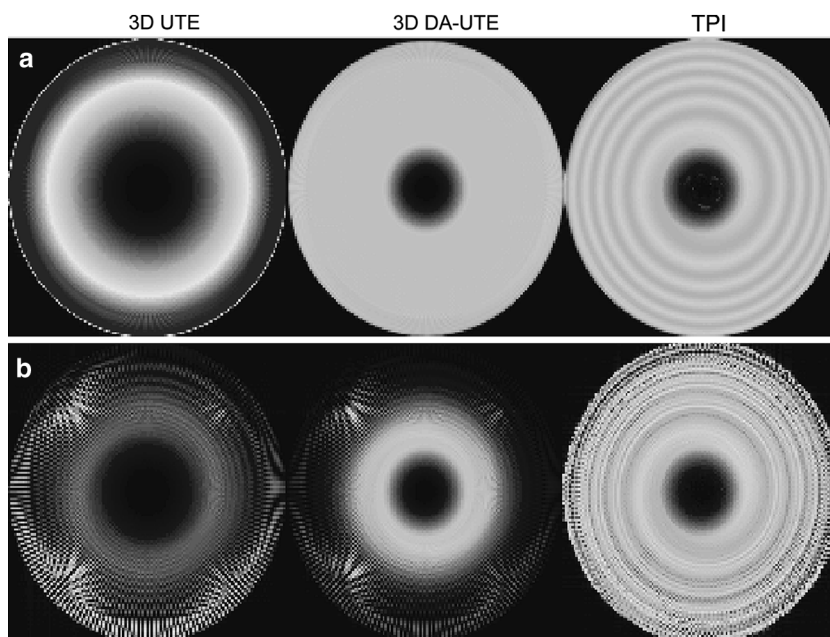


**Fig. 3** Signal magnitude at  $k$ -space center plotted against number of projections during free-breathing imaging at TE of 0.07 ms. Views corresponding to *green* and *red* segments were used to reconstruct images at expiration and inspiration, respectively

gating. Assessment of the DC signal changes resulting from respiratory motion was made using the coil element of the body matrix near the liver-lung interface, which shows the highest sensitivity toward the respiratory motion. Fig. 3 shows a temporally smoothed DC signal, in which the respiratory cycle can be clearly observed. Thresholds were manually chosen at approximately one-third of each respiratory cycle to reconstruct lung images at inspiratory and expiratory phases.

### In vivo experiments

All studies were performed during free breathing using a clinical 1.5 T MRI system (MAGNETOM Avanto; Siemens Healthcare, Erlangen, Germany). For signal reception, a six-element body array and six elements of a spine array were used in all studies. Six healthy volunteers (one female, five male) were examined in supine position. In accordance with institutional regulations, written informed consent was obtained from each volunteer prior to the study. Non-rebreathing face masks were used for air supply. The volunteers were instructed to completely exhale during breathing. The breathing gas consisted of either room air or 100 % oxygen, and was delivered through a face mask. After the gas was switched, a 5-min waiting time was implemented to avoid wash-in effects.

The excitation consisted of a non-selective hard pulse  $50 \mu\text{s}$  in duration. Empirical research indicated that a flip-angle of  $10^\circ$  and TR of 7 ms were a good compromise between  $T_1$  weighting to detect changes in  $T_1$ , fast imaging, and sufficient SNR for simultaneous  $T_2^*$  quantification. Within each TR, two readouts were acquired. For subsequent TRs, the start of acquisition was shifted by  $530 \mu\text{s}$  to yield echo times of 0.07/1.2 ms and 0.6/1.73 ms, respectively. A field of view (FOV) of  $50 \times 50 \times 50$  cm and 64 readout points, with a readout window length of  $850 \mu\text{s}$ , were used to achieve an isotropic resolution of  $3.9 \times 3.9 \times 3.9 \text{ mm}^3$ .

A read oversampling of 6 was used to prevent aliasing artefacts in the readout direction. The trajectories were linearly sampled up to a fraction  $p = 0.49$ , and then twisted to



yield a cone with  $\Phi = 8^\circ$ . The number of projections acquired was  $14 \times 10^4$  ( $7 \times 10^4$  per double-echo), leading to a total acquisition time of 16 min 20 s for each gas.

Image reconstruction was performed offline using MATLAB software (MathWorks, Natick, MA). The k-space data were gridded using a Kaiser-Bessel interpolation kernel [23] and Fourier-transformed using fast Fourier transform.

The signal intensity time course for each pixel was monoexponentially fitted over the four echo times (TE) using the following equation:  $S(\text{TE}) = \text{SI} \cdot \exp(-\text{TE}/T_2^*)$ , where SI is the relative  $T_1$ -weighted spin density. To demonstrate the feasibility of the method,  $T_2^*$  and relative spin density values were compared for one coronal posterior slice far from the heart and one coronal anterior slice through the heart.  $T_2^*$  and SI values were determined from ROIs drawn in the whole right and left lung. Large values from the vessels that would skew the distribution of parenchymal  $T_2^*$  values were excluded using a manually selected threshold based on SI.

Relative percentage signal change  $\Delta\text{SI}_{\text{gas}}$  and  $\Delta\text{SI}_{\text{res}}$  are used to express changes in relative SI due to the respiratory gas and to the volumetric change

$$\Delta\text{SI}_{\text{gas}} = 100 \cdot \frac{\text{SI}_{\text{O}_2} - \text{SI}_{\text{air}}}{\text{SI}_{\text{O}_2}}$$

$$\Delta\text{SI}_{\text{res}} = 100 \cdot \frac{\text{SI}_{\text{Ex}} - \text{SI}_{\text{In}}}{\text{SI}_{\text{Ex}}}$$

with signal intensity with subjects breathing pure oxygen ( $\text{SI}_{\text{O}_2}$ ) and room air ( $\text{SI}_{\text{air}}$ ) at inspiration ( $\text{SI}_{\text{In}}$ ) and expiration ( $\text{SI}_{\text{Ex}}$ ).

The relative percentage change  $\Delta T_2^*$  is calculated as

$$\Delta T_2^* = 100 \cdot \frac{T_{2,\text{air}}^* - T_{2,\text{O}_2}^*}{T_{2,\text{air}}^*}$$

with  $T_2^*$  during breathing of room air ( $T_{2,\text{air}}^*$ ) and oxygen ( $T_{2,\text{O}_2}^*$ ).

$\Delta T_2^*$  can be expressed as

$$\frac{1}{T_2^*} = \frac{1}{T_2} + \gamma B_0 + \gamma \chi B_0$$

where  $T_2$  is the conventional transverse relaxation time, and  $\gamma \Delta B_0$  and  $\gamma \chi B_0$  are changes in frequency due to macroscopic magnetic field gradients and mesoscopic magnetic field inhomogeneities dependent on the magnetic susceptibility  $\chi$  (e.g., at gas-tissue interfaces). Therefore, the difference of inverse  $T_2^*$  measured at room air and 100 % oxygen

$$\Delta \left( \frac{1}{T_2^*} \right) = \Delta \left( \frac{1}{T_{2,\text{O}_2}^*} - \frac{1}{T_{2,\text{air}}^*} \right) = \gamma (\chi_{\text{O}_2} - \chi_{\text{air}}) B_0$$

reflects changes in susceptibility due to an increased oxygen concentration in the alveoli, and thus was used to calculate

difference maps with the assumption that this measure reflects lung function better than direct  $T_2^*$  differences.

## Results

Measurements from all subjects were completed successfully, and images of expiratory and inspiratory states were reconstructed using DC gating, with a mean number of 24,077 and 20,284 projections for expiratory and inspiratory phases, respectively. Using the Nyquist criterion, this results in undersampling factors of 1.07 and 1.27.

Table 1 provides  $T_2^*$  values and percentage changes in  $T_1$ -weighted SI of two representative coronal slices for each subject and the corresponding mean values with 95 % confidence intervals (CIs).

### Regional $T_2^*$ mapping

Figure 4 shows typical  $T_2^*$  maps in expiratory and inspiratory phases for subjects breathing 100 % oxygen as well as room air. For all subjects,  $T_2^*$  was highest during breathing room air in expiratory state, and decreased approximately 10.1 % (95 % CI 8.9–11.3 %) when breathing pure oxygen in the posterior slice. The average  $T_2^*$  was 2.10 ( $\pm 0.19$ ) ms when breathing room air and 1.89 ( $\pm 0.16$ ) ms when breathing oxygen in expiration. In all subjects, a difference in  $T_2^*$  between the two respiratory phases was observed.  $T_2^*$  decreased by 5.7 % (95 % CI 3.7–7.7 %) from expiratory to inspiratory phase.

For the expiratory state, the  $T_2^*$  values in the anterior slice near the heart were lower for all subjects (3.6 %, 95 % CI 2.3–5.0 %), but showed a comparable decrease of 10.2 % (95 % CI 9.6–10.7 %) when subjects were breathing pure oxygen.

Figure 5 displays representative subtraction maps of inverse  $T_2^*$  in the expiratory state as a result of switching the breathing gas from room air to pure oxygen, which directly illustrates the differences arising from altered susceptibility of the two breathing gases. A change in  $T_2^*$  in the expected range of 10 % can be observed in all slices.

### Regional spin density mapping

Figure 6 shows the  $T_1$ -weighted images of the posterior and anterior coronal slice for one subject. The SI increased in both respiratory phases when subjects were breathing pure oxygen. For the posterior slice, the increase was approximately 11.2 % (95 % CI 10.42–12.05 %) in expiration and 12.7 % (95 % CI 10.0–15.4 %) in inspiration. For the anterior slice, the increase was approximately 11.6 % (95 % CI 10.9–12.3 %) in expiration and 11.9 % (95 % CI 7.5–16.4 %) in inspiration.

**Table 1** Quantitative  $T_2^*$  values (in ms) with mean  $\pm$  deviation at inspiration (In) and expiration (Ex) with subjects breathing room air (Air) and pure oxygen ( $O_2$ ), as well as the relative percentage signal

changes due to respiratory gas ( $\Delta SI_{\text{gas}}$ ) at expiration and volumetric change ( $\Delta SI_{\text{res}}$ ) in coronal slices (posterior and anterior), for each subject

	In, Air	Ex, Air	In, $O_2$	Ex, $O_2$	$T_2^*$ [%]	$\Delta SI_{\text{gas}}$ [%]	$\Delta SI_{\text{res}}$ [%]
<i>Coronal posterior slice</i>							
Subject 1	2.15 $\pm$ 0.45	2.37 $\pm$ 0.41	1.89 $\pm$ 0.43	2.10 $\pm$ 0.38	11.4	10.2	42.2
Subject 2	2.11 $\pm$ 0.44	2.22 $\pm$ 0.42	1.83 $\pm$ 0.39	2.01 $\pm$ 0.36	9.5	10.6	22.2
Subject 3	1.95 $\pm$ 0.50	2.10 $\pm$ 0.45	1.73 $\pm$ 0.45	1.85 $\pm$ 0.41	11.9	11.8	22.1
Subject 4	2.11 $\pm$ 0.51	2.20 $\pm$ 0.43	1.85 $\pm$ 0.45	1.98 $\pm$ 0.37	10.0	12.5	20.1
Subject 5	1.79 $\pm$ 0.41	1.87 $\pm$ 0.39	1.65 $\pm$ 0.34	1.71 $\pm$ 0.38	8.6	11.5	24.8
Subject 6	1.77 $\pm$ 0.40	1.85 $\pm$ 0.40	1.61 $\pm$ 0.33	1.68 $\pm$ 0.35	9.2	10.8	27.8
Mean	1.98 $\pm$ 0.15	2.10 $\pm$ 0.19	1.76 $\pm$ 0.10	1.89 $\pm$ 0.16	10.1	11.2	26.5
95 % CI	1.89–2.10	1.95–2.25	1.67–1.84	1.76–2.01	8.87–11.3	10.42–12.05	18.78–34.29
<i>Coronal anterior slice</i>							
Subject 1	2.13 $\pm$ 0.52	2.25 $\pm$ 0.42	1.95 $\pm$ 0.50	2.00 $\pm$ 0.41	11.1	10.6	41.5
Subject 2	2.04 $\pm$ 0.44	2.12 $\pm$ 0.38	1.81 $\pm$ 0.43	1.91 $\pm$ 0.36	9.9	11.3	15.2
Subject 3	1.88 $\pm$ 0.52	2.01 $\pm$ 0.44	1.68 $\pm$ 0.50	1.80 $\pm$ 0.44	10.4	11.4	15.5
Subject 4	2.05 $\pm$ 0.43	2.11 $\pm$ 0.44	1.80 $\pm$ 0.43	1.89 $\pm$ 0.42	10.4	12.7	18.5
Subject 5	1.77 $\pm$ 0.39	1.84 $\pm$ 0.39	1.59 $\pm$ 0.31	1.66 $\pm$ 0.39	9.8	12.3	21.1
Subject 6	1.78 $\pm$ 0.40	1.81 $\pm$ 0.36	1.65 $\pm$ 0.40	1.64 $\pm$ 0.39	9.4	11.3	29.8
Mean	1.94 $\pm$ 0.14	2.02 $\pm$ 0.15	1.74 $\pm$ 0.12	1.81 $\pm$ 0.13	10.2	11.6	23.5
95 % CI	1.83–2.05	1.90–2.15	1.65–1.84	1.67–1.88	9.60–10.74	10.87–12.33	13.63–33.40

The percentage change  $\Delta T_2^*$  is added for the expiratory phase as well as the average values with standard deviation and the 95 % confidence intervals of the mean values

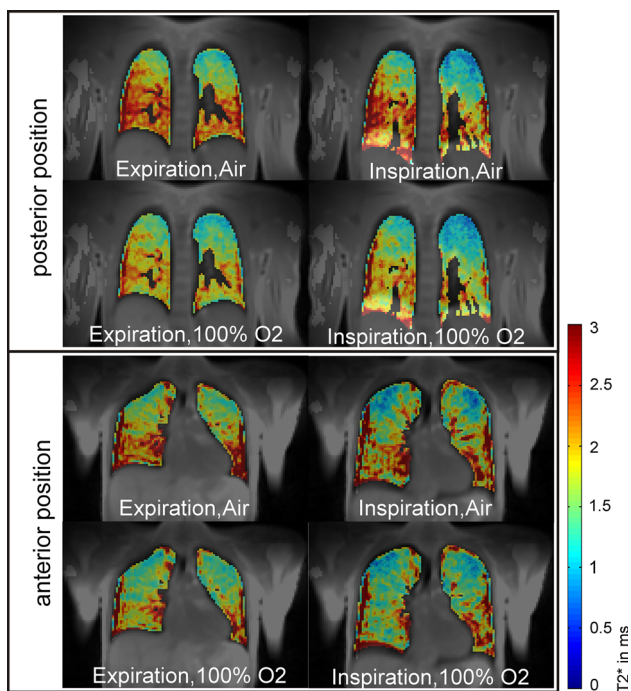


**Fig. 4**  $T_2^*$  maps (in ms) for one anterior and one posterior coronal slice at expiration and inspiration of room air and pure oxygen

Percentage-change maps of  $T_1$ -weighted images in different orientations are displayed in Fig. 7. This directly and quantitatively displays the transfer of oxygen

into the blood as the result of ventilation, perfusion, and diffusion.

SI was also compared between the two respiratory phases. SI was highest in the expiratory state and, as expected, changed significantly with lung volume. In the posterior slice, changes of approximately 26.5 % (95 % CI 18.8–34.3 %) were observed when subjects were breathing room air and approximately 25.3 % (95 % CI 17.7–32.9 %) with subjects breathing pure oxygen. In the anterior the slice, signal intensity changed by 23.5 % (95 % CI 13.6–33.4) when subjects were breathing room air and 23.15 % (95 % CI 13.2–33.1 %) with subjects breathing pure oxygen.

Between anterior and posterior slices, a difference in signal intensity of 18.0 % (95 % CI 15.2–20.8) in expiration and 14.9 % (95 % CI 11.3–18.4) in inspiration was observed.

## Discussion

In this study,  $T_1$ -weighted imaging and  $T_2^*$  quantification were combined in a multiparametric evaluation of lung function in 3D using a clinical 1.5T scanner.

The 3D radial readout is based on a TPI sequence that provides ultrashort echo times and optimal scan efficiency, which allows for simultaneous quantitative  $T_2^*$  mapping

**Fig. 5** Subtraction maps  $\Delta(1/T_2^*)$  of the expiratory phase between the two breathing gases in coronal (a), transverse (b), and sagittal (c) orientation

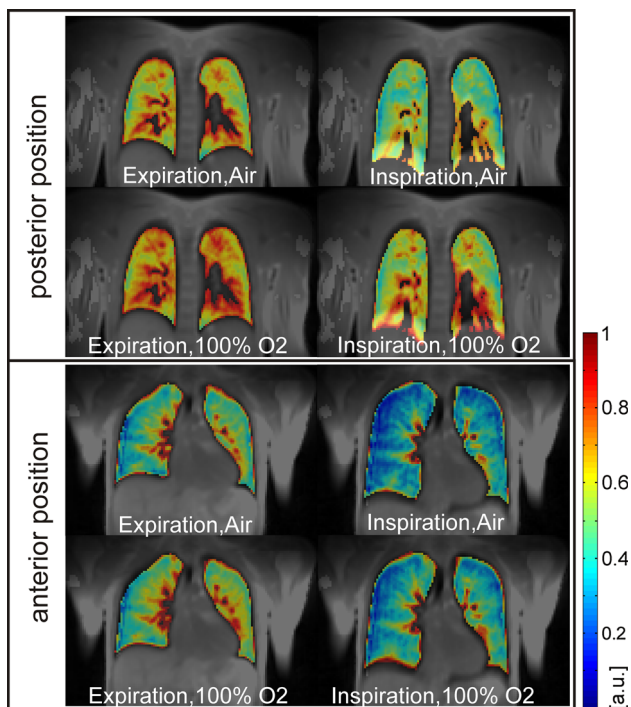
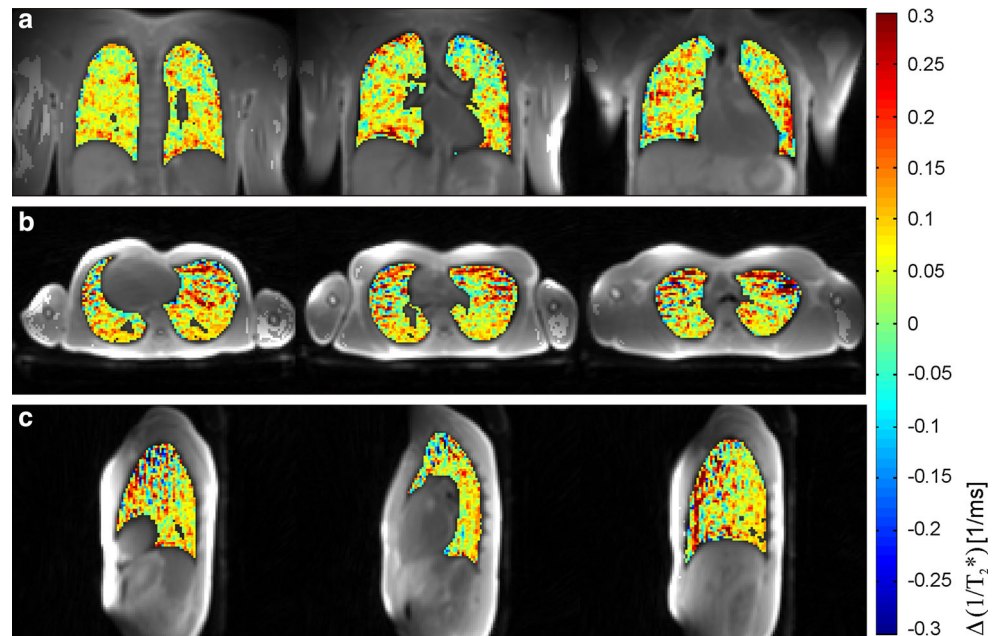


**Fig. 6**  $T_1$ -weighted images of one anterior and one posterior coronal slice at expiration and inspiration for subjects breathing room air and 100 % oxygen

and  $T_1$ -weighted SI mapping of the whole lung. In contrast to the original TPI, only one trajectory was implemented, which simplified the correction of gradient imperfections. As can be seen from Fig. 2, the sequence that was employed provides almost constant sampling density, even for a low number of projections. However, it does show a

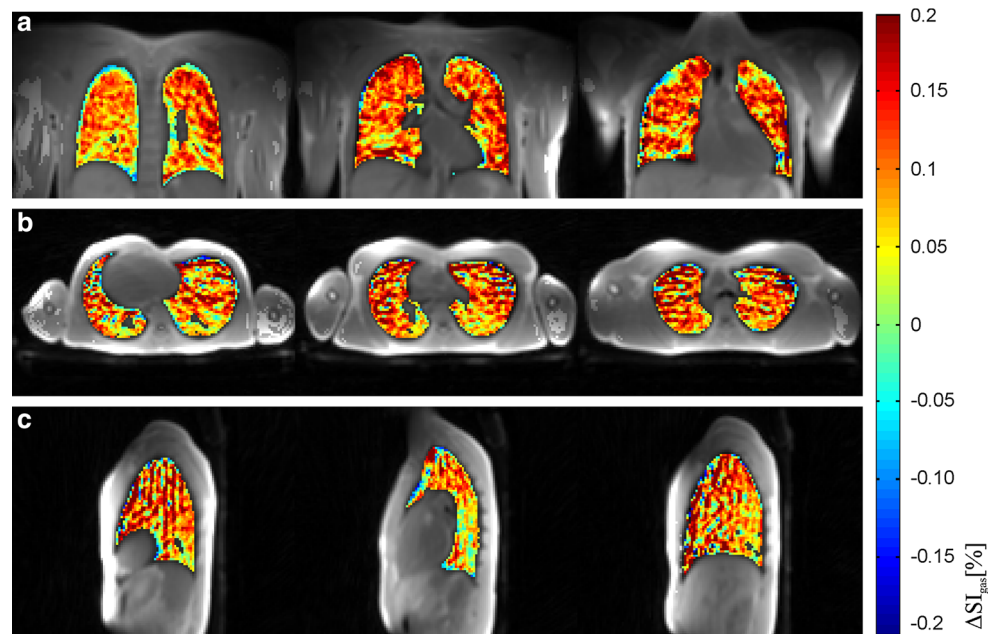
moderate wave pattern, which can be attributed to locations where the rotated cones intersect and thus deviate slightly from a perfectly constant DCF.

The use of quasi-randomly distributed projection angles enabled sequence capacity for retrospective respiratory self-gating. In all subjects, the DC signal reflected the respiratory motion, and data from expiratory and inspiratory phases were selected retrospectively to calculate  $T_2^*$  maps as well as  $T_1$ -weighted SI maps in 3D. As demonstrated, the number of  $7 \times 10^4$  projections acquired was sufficient to provide nearly fully sampled inspiratory and expiratory data in all subjects.

Kruger et al. [7] used 38,000 projections and a total scan time of 5–6 min for  $T_1$ -weighted oxygen-enhanced (OE) lung imaging with a 3D radial UTE sequence and real-time prospective gating to end-expiration. In contrast, with the self-gated approach proposed in this study, two double readouts with 70,000 projections were acquired in approximately 16 min. This allows for the possibility of retrospective reconstruction to arbitrary breathing states (e.g., expiration and inspiration). Moreover, in addition to the  $T_1$  weighted images that are available, the multi-echo sequence also provides the possibility for quantitative  $T_2^*$  mapping.

To yield appropriate echo times for the  $T_2^*$  assessment, a high receiver bandwidth and two interleaved double-echo readouts were used. Since multiple echoes are acquired within two subsequent TRs, misregistration between different echoes is avoided. Because the center of the k-space is heavily oversampled, this method is insensitive to major motion artefacts. As can be seen in the anterior slices through the heart (Figs. 4, 6), artefacts originating from cardiac motion are sufficiently suppressed.

**Fig. 7** Percentage-change maps  $\Delta SI_{\text{gas}}$  of  $T_1$ -weighted images of expiratory phase in coronal (a), transverse (b), and sagittal (c) orientation



The echo times were chosen such that the oxygen-induced  $T_2^*$  changes could be detected. This required the acquisition of echoes at TEs where fat and water protons are in different in-phase and out-of-phase states, which leads to incorrect  $T_2^*$  values in pixels containing both fat and water protons that are assumed not to be found in the lungs.

Evaluation in all slices and orientations was beyond the scope of this paper, and as a proof-of-principle,  $T_2^*$  ratios and relative SI were determined only in one posterior and one anterior coronal slice.  $T_2^*$  maps, as shown in Fig. 4, were calculated for all subjects for the different breathing gases and breathing states. As can be seen, a dispersion of  $T_2^*$  from lower to higher values from upper to lower lung was observed in all subjects, which may be attributable to a more highly perfused lower lung in the supine position, as the subtraction images in Fig. 5 show a more uniform distribution, which indicates a relatively uniform ventilation of the lung in the healthy subjects. Therefore, it can be assumed that this  $T_2^*$  gradient refers to a gravitational or  $T_2$  effect.

The expected changes in  $T_2^*$  and relative SI within different respiratory phases and different breathing gases were detected in all subjects. As can be seen in Table 1, mean  $T_2^*$  decreased 8.6–11.4 % in the posterior slice and 9.4–11.1 % in the anterior slice in expiration after breathing pure oxygen. This is consistent with results reported by Pracht et al. [10], which indicated an approximate 10 % decrease in  $T_2^*$  in a single expiratory slice during breath-hold. The authors posited that the effect of increased oxygen saturation in the blood could be neglected, as expected blood susceptibility changes were smaller than 1 %. Thus, under

the assumption that  $T_2^*$  is not altered by saturated hemoglobin (e.g., due to increased perfusion), the regional  $T_2^*$  changes can be directly attributed to ventilated areas.

In expiration, a decrease in  $T_2^*$  (1.6–5.1 %) between the posterior and anterior slices was observed in all subjects. This was not observed for the inspiratory phase, however, which may be attributable to low SNR.

In the posterior slice far from the heart, a mean change in  $T_2^*$  of 5.8 % was observed between expiratory and inspiratory states. Therefore, a smaller change in  $T_2^*$  was observed than when measuring during breath-hold [11]. This is consistent with the work of Yu et al. [24], who reported minor changes in  $T_2^*$  (<0.1 ms) between the two respiratory phases when data was acquired during free breathing. The same decrease during breathing was not observed in the anterior slice, which may be due to low SNR in inspiration or weaker breathing in the anterior lung.

In order to generate subtraction maps for the two breathing gases, the inverse ratios  $\Delta(1/T_2^*)$  were used rather than  $\Delta T_2^*$ , with the expectation that this would directly display the susceptibility change due to an increased amount of oxygen in the breathing gas, thereby providing more accurate information regarding ventilation. Since the images originate from two subsequent measurements, they show slight misregistration artefacts, and additional studies are needed for image registration to avoid misinterpretation.

The expiratory  $T_1$ -weighted images showed increases in signal intensity of 10.2–12.5 % in the posterior and 10.6–12.7 % in the anterior slice when subjects were breathing pure oxygen, which is in good agreement with other findings [1, 5]. These changes, which are best seen



in percentage subtraction maps such as those displayed in Fig. 7, show the oxygen content in the lung resulting from ventilation, perfusion, and diffusion. As was noted with the  $T_2^*$  subtraction maps, these images also suffer from minor misinterpretation due to motion. However, a key feature of respiratory self-gating is that  $T_2^*$  and SI maps are already registered to the same respiratory state, and thus regional changes can be observed on a pixel-by-pixel basis.

Furthermore, a decrease in signal intensity between posterior and anterior slices was clearly seen in all subjects. This demonstrates the vertical gradient in lung tissue density caused by gravity, the so-called Slinky effect [25].

Similar to the findings reported by Hatabu and Theilmann [11, 12] an increase in signal intensity was detected at maximum expiration compared to inspiration. Signal changes in the posterior slice ranged from 20.1 %–42.2 % among the six subjects. These changes are attributable to the increased gas fraction in the lung during inspiration, resulting in decreased lung density, while tissue and blood volumes remain constant. In the anterior slice, changes in signal intensity ranged from 15.2–41.5 %. In some subjects, the degree of change was lower in the anterior slice than the posterior slice, which will require further investigation. The application of advanced 3D registration algorithms in mapping inspiratory and expiratory states to a joint state is expected to provide quantitative information on lung volume, capacity, and lung expansion.

The chief drawback to the approach presented here is that the scan time is still relatively long, with approximately 16 min per breathing gas required to robustly extract all of the parameters in 3D, as discussed above. Strategies such as compressed sensing [26] may help to reduce imaging time by a factor of 1.5–2.0, with no loss in functional information. Additional study limitations include the large amount of data acquired and the relatively long reconstruction times associated with the non-Cartesian imaging module.

The scanner's body/spine receiver coil array provided sufficient sensitivity for all cases. However, the general applicability of this approach must be tested, especially in patients with more irregular or shallow breathing. It is important to note that even in subjects with very irregular breathing, there is still the possibility of reconstructing the data to an intermediate breathing state by averaging over all of the projections. This approach will lead to temporal blurring, particularly at the lung-liver interface, but still may provide the desired functional information over a wide area in the lung.

In future studies, the approach presented here will be clinically evaluated towards improved diagnosis of several lung diseases, with a focus on the availability of joint

information regarding ventilation, OTF, and lung expansion/capacity.

## Conclusions

In this work, the feasibility of the simultaneous measurement of quantitative  $T_2^*$  and  $T_1$ -weighted images in 3D at different breathing phases was demonstrated in a proof-of-principle study. A reduction in  $T_2^*$  and an increase in  $T_1$ -weighted signal intensity when subjects were breathing oxygen versus room air was consistent with data reported in the literature. This method also provides information regarding lung expansion and gas volume fraction in 3D. Further evaluation of all slices is necessary to verify these results and to characterize the value of the 3D data. Future studies are needed to investigate the clinical applicability and diagnostic value of this approach in various pulmonary diseases.

**Conflict of interest** The authors each declare that they have no conflict of interest. The authors have no financial relationship with the organization that sponsored the research.

**Ethical standards** This manuscript contains no clinical studies or patient data.

## References

1. Edelman R, Hatabu H, Tadamura E, Li W, Prasad PV (1996) Noninvasive assessment of regional ventilation in the human lung using oxygen enhanced magnetic resonance imaging. *Nat Med* 2:1236–1239
2. Jakob PM, Wang T, Schultz G, Hebestreit H, Hebestreit A, Hahn D (2004) Assessment of human pulmonary function using oxygen-enhanced T1 imaging in patients with cystic fibrosis. *Magn Reson Med* 51:1009–1016
3. Nakagawa T, Sakuma H, Murashima S, Ishida N, Matsumura K, Takeda K (2001) Pulmonary ventilation-perfusion MR imaging in clinical patients. *J Magn Reson Med* 14:419–424
4. Chen Q, Jakob PM, Griswold MA, Levin DL, Hatabu H, Edelman RR (1998) Oxygen enhanced MR ventilation imaging of the lung. *Magn Reson Mater Phy* 7:153–161
5. Arnold JFT, Kotas M, Fidler F, Pracht ED, Flentje M, Jakob PM (2007) Quantitative regional oxygen transfer imaging of the human lung. *J Magn Reson Imaging* 26:637–645
6. MacFall JR, Halaweish A, Foster WM, Moon RE, MacIntyre NR, Soher B, Charles HC (2013) Evaluation of free breathing Ultra-Short TE 3D MRI for oxygen enhanced imaging of the human lung. In: Proceedings of the 21th scientific meeting, International Society for Magnetic Resonance in medicine, Salt Lake City, p 1491
7. Kruger SJ, Johnson KM, Fain SB, Cadman RV, Bell LC, Nagle SK (2012) Oxygen enhanced lung MRI using 3D radial UTE SPGR in humans. In: Proceedings of the 21th scientific meeting, International Society for Magnetic Resonance in medicine, Melbourne, p 1344
8. Takahashi M, Togao O, Obara M, van Cauteren M, Doi S, Ohno YS, Kuro-o M, Malloy C, Hsia C, Dimitrov I (2010) Ultra-short

- echo time (UTE) MR imaging of the lung: comparison between normal and emphysematous lungs in mutant mice. *J Magn Reson Imaging* 32:326–333
9. Ohno Y, Nishio M, Koyama H, Takahashi M, Yoshikawa T, Matsumoto S, Takenaka D, Kyotani K, Aoyama N, Kawamitsu H, Obara M, van Cauteren M, Sugimura K (2012) T2\* Measurements of 3 T MRI with Ultra-Short TE: Capability of assessments for pulmonary functional loss and disease severity in patients with Connective Tissue Disease (CTD). In: Proceedings of the 20th scientific meeting, International Society for Magnetic Resonance in Medicine, Melbourne, p 3967
  10. Pracht ED, Arnold JFT, Wang T, Jakob PM (2005) Oxygen-enhanced proton imaging of the human lung using T2\*. *Magn Reson Med* 53:1193–1196
  11. Theilmann RJ, Arai TJ, Samiee A, Dubowitz D, Hopkins S, Buxton RB, Prisk GK (2009) Quantitative MRI measurement of lung density must account for the change in T2\* with lung inflation. *J Magn Reson Imaging* 30:527–534
  12. Hatabu H, Alsop DC, Listerud J, Bonnet M, Geftter WB (1999) T2\* and proton density measurement of normal human lung parenchyma using submillisecond echo time gradient echo magnetic resonance imaging. *Eur J Radiol* 29:245–252
  13. Bergin CJ, Pauly JM, Macovski A (1991) Lung parenchyma: projection reconstruction MR imaging. *Radiology* 179:777–781
  14. Togao O, Ohno Y, Dimitrov I, Hsia CC, Takahashi M (2011) Ventilation/perfusion imaging of the lung using ultra short echo time (UTE) MRI in an animal model of pulmonary embolism. *J Magn Reson Imaging* 34:539–546
  15. Liao JR, Pauly JM, Brosnan TJ, Pelc NJ (1997) Reduction of motion artifacts in Cine MRI using variable-density spiral trajectories. *Magn Reson Med* 37:569–575
  16. Johnson KM, Fain SB, Schiebler ML, Nagle S (2012) Optimized 3D ultra short echo time pulmonary MRI. *Magn Reson Med* 70:1241–1250
  17. Boada FE, Gillen JS, Shen GX, Chang SY, Thulborn KR (1997) Fast three dimensional sodium imaging. *Magn Reson Med* 37:706–715
  18. Weick S, Breuer FA, Ehses P, Völker M, Hintze C, Biederer J, Jakob PM (2013) DC-gated high resolution three-dimensional lung imaging during free-breathing. *J Magn Reson Imaging* 37:727–732
  19. Krämer P, Konstandin S, Heilmann M, Schad LR (2011) 3D radial Twisted projection imaging for DCE-MRI with variable flip angles. In: Proceedings of the 19th scientific meeting, International Society for Magnetic Resonance in medicine, Montreal, p 2055
  20. Chan RW, Ramsay EA, Cunningham CH, Plewes DB (2009) Temporal stability of adaptive 3D Radial MRI using multidimensional golden means. *Magn Reson Med* 61:354–363
  21. Pipe JG, Menon P (1999) Sampling density compensation in MRI: rationale and an iterative numerical solution. *Magn Reson Med* 41:179–186
  22. Brau CS, Brittain JH (2006) Generalized self-navigated motion detection technique: preliminary investigation in abdominal imaging. *Magn Reson Med* 55:263–270
  23. Fessler JA (2007) On NUFFT-based gridding for non-Cartesian MRI. *J Magn Reson* 188:191–195
  24. Yu J, Xue Y, Song HK (2011) Comparison of lung T2\* during free-breathing at 1.5 T and 3.0 T with ultrashort echo time imaging. *Magn Reson Med* 66:248–254
  25. Hopkins SR, Henderson AC, Levin DL, Yamada K, Arai T, Buxton RB, Prisk GK (2007) Vertical gradients in regional lung density and perfusion in the supine human lung: the Slinky effect. *J Appl Physiol* 103:240–248
  26. Lustig M, Donoho DL, Pauly JM (2007) Sparse MRI: the application of compressed sensing for rapid MR imaging. *Magn Reson Med* 58:1182–1195